# Anisotropy origins of coefficient of friction and scratch hardness in nano scratching monocrystalline copper

Huan Liu [a], Yongbo Guo [a,*], Pengyue Zhao [b,c], Duo Li [a,e], Shaoyuan Sun [d]

[a] Center for Precision Engineering, Harbin Institute of Technology, Harbin 150001, China
[b] Center of Ultra-Precision Optoelectronic Instrumentation Engineering, Harbin Institute of Technology, Harbin 150001, China
[c] Key Lab of Ultra-precision Intelligent Instrumentation (Harbin Institute of Technology), Ministry of Industry and Information Technology, Harbin 150080, China
[d] Center for Analysis and Measurement Harbin Institute of Technology, Harbin 150001, China
[e] State Key Laboratory of Applied Optics, Changchun Institute of Optics, Fine Mechanics and Physics, Chinese Academy of Sciences, Changchun, Jilin 130033, China

## ARTICLE INFO

## ABSTRACT

The monocrystalline Cu material mechanical properties at the micro and nano scale show complex anisotropy and size effects. However, the anisotropy of scratch hardness and coefficient of friction (COF) in micro-nano scratching monocrystalline Cu has not been well explained. In this paper, we conducted the nano-scratching experiments and corresponding molecular dynamics (MD) simulation under ramp normal force mode along two representative crystal orientations thereby investigating the anisotropy origins of scratch hardness and COF. The research results indicate that, for monocrystalline Cu materials, the scratch hardness and COF are closely related to the atomic slip resistance $F_{slip}$ caused by the activated <1 1 0> {1 1 1} slip systems.

## 1. Introduction

Nano-scratching test is an important method to study near-surface mechanical properties, such as friction behavior [1,2], wear mechanism [3,4], grinding [5,6], and chemical mechanical polishing process [7–9]. The nano-scratching test is conducted by a hard submicron-sized tip, which scratches the specimen surface with nano-scale press-in depth under the combining action of normal load and lateral movement. In particular, during the ramp force mode nano-scratching process, the normal force and the scratch depth increase with the scratch distance. This nano-scratching test can be employed to investigate the size effects of friction, scratch hardness, and plastic deformation behavior caused by scratching [10,11]. Meanwhile, employing the MD method to simulate the nano-scratching process can make up for the shortcomings of nano-scratching experiments that are difficult to analyze the motion law of atoms inside the material in real time. At present, MD simulation and nano-scratching tests are the main means to investigate the nano-scratching mechanism.

Nanoindentation and scratch hardness are both important parameters to characterize the near-surface mechanical properties of materials. Scholars have been trying to construct an intrinsic relationship between indentation and scratch hardness [12–15]. The indentation hardness obtained at any location on a homogeneous material surface should be

the same. However, for monocrystal Cu material, the scratch hardness exhibits anisotropy when scratching along different directions on the same specimen surface. Brookes et al. [16] found that the ratios of indentation hardness and scratch hardness are 1.71 and 1.03, respectively, when scratching along $[1\ 1\ \overline{2}]$ and $[\overline{1}\ \overline{1}\ 2]$ on monocrystalline Cu (1 1 1) surface. The anisotropy of scratch hardness has also been found in the nano-scratching process of other crystals [17]. In addition, the COF in nano-scratching is also closely related to the scratch direction and specimen surface crystal orientation. Zhang et al. [18] carried out single-point turning experiments on monocrystalline Cu (0 0 1), (1 1 0), and (1 1 1) surfaces and the experimental results show that the COF changes with machining direction and specimen surface crystal orientation. At present, the anisotropy origin for COF and scratch hardness is unclear, and there is no consensus theory to analyze the scratch hardness and COF anisotropy of crystalline materials.

The nano-scratching process is extremely complex, and the COF and scratch hardness are affected by many factors, such as temperature [19], surface roughness [20], and the scratch-tip-size effect [21]. Meanwhile, different nano-scratching deformation behaviors, such as rubbing, ploughing, chip and fracture, usually correspond to different COF and scratch hardness [22,23]. Therefore, the material plastic deformation behavior during the scratching process has a non-negligible effect on the COF and scratch hardness. For the monocrystalline Cu material, the

---

plastic deformation caused by scratching will show anisotropy. Zhu et al. [24] conducted the monocrystalline Cu nano-scratching experiments and corresponding crystal plasticity finite element simulation on the (0 0 1) crystalline surface along with five different scratch directions. They found that the pile-up and scratch depth are closely related to the scratch directions and speed. Meanwhile, the crystal plasticity finite element simulation results for scratching monocrystalline Cu (0 0 1) crystalline surface indicate that the scratch hardness has a significant impact on the wear coefficient [25]. Wang et al. [26] found the scratch morphologies is different when scratching on (0 0 1), (1 1 0), and (1 1 1) crystal surface, with the help of crystal plasticity finite element simulation and nano-scratching experiments. Sharma et al. [27] conducted the MD simulation of nano-cutting monocrystalline Cu under six crystal orientations and found that the ploughing height, cutting force, and dislocation density all exhibit anisotropy. Hu et al. [28] investigated the anisotropy of monocrystalline Cu stick-slip friction by MD methods. The simulation results show that the critical frictional force depends on the crystal orientations. Xu et al. [29] employed a $CeO_2$ tip to carry out the nano-scratching monocrystalline Cu experiments under constant and ramp normal force mode. They found that the COF changed with the scratch depth, showing a trend of decreasing first, then increasing, and finally stabilizing. Tsybenko et al. [12] found that, during the process of nano-scratching monocrystalline Cu, the scratch hardness first decreases and then increases with the increase of normal load. The existing literature indicates that the scratching deformation behavior, COF, and scratch hardness all exhibit anisotropy during the nano-scratching monocrystalline Cu process. However, the intrinsic relationship between nano-scratching deformation behavior, scratch hardness, and COF has not been investigated. In this paper, from the perspective of the monocrystalline copper atomic movement, the atomic slip resistance $F_{slip}$ in nano-scratching was first proposed to explain the anisotropy origin of scratch hardness and COF under different nano-scratching deformation behaviors.

This paper chooses the scratch direction of (2 0 5)[5 0 $\overline{2}$] and (2 0 5)[$\overline{5}$ 0 2] as the representative research objects to investigate the anisotropy origins of COF and scratch hardness. The reason is that the nano-scratching deformation behaviors for (2 0 5)[5 0 $\overline{2}$] and (2

0 5)[$\overline{5}$ 0 2] scratch directions are chip and ploughing, respectively, due to the difference in the activated < 1 1 0{1 1 1} slip systems [30,31]. These two representative scratch directions with significant differences in scratching behavior can more clearly reveal the origin of anisotropy of monocrystalline Cu materials in the nano scratching process. In this paper, the nano-scratching experiments with ramp normal force and corresponding MD simulations were conducted along the scratch direction (2 0 5)[5 0 $\overline{2}$] and (2 0 5)[$\overline{5}$ 0 2], and the nano-indentation tests on the monocrystalline Cu surface with Miller index (2 0 5) were carried out to obtain the nano-indentation hardness. Meanwhile, the scratch hardness and COF anisotropy and the reason for the difference between indentation hardness and scratch hardness can be analyzed by the atomic slip resistance $F_{slip}$ caused by the activated < 1 1 0 > {1 1 1} slip system. Combined with our previous researches, a more comprehensive understanding for the effect of monocrystalline Cu material characteristics on the nano scratching process is presented in this paper.

## 2. Methods

### 2.1. Nano scratching experiments and corresponding MD simulations

Nano Indenter G200 was employed to conduct the nano-scratching experiments along the scratch directions [5 0 $\overline{2}$](2 0 5) and [$\overline{5}$ 0 2](2 0 5). In this paper, [] represents the specific crystal orientation, < > represents the crystal orientation families, () represents the specific crystal plane, {} represents the crystal plane families. As shown in Fig. 1 (a), the nano-scratching experiments consist of three steps, namely prescan, scratch, and postscan [29]. Firstly, in prescan, a constant normal force of 2 μN was employed to get the initial surface information of the monocrystalline Cu specimen, thereby correcting the scratch depth and residual depth. Then, the diamond indenter turned back and scratched the Cu surface with 2 μm/s. The ramp force is the normal force that uniformly increases with the scratching time in nano scratching process, as shown by the blue line during the scratch stage in Fig. 1(a). The ramp rate for normal force is 0.04 mN/s. The physical process corresponding to the platform for scratch distance curve in scratch stage is that the tip moves vertically away from the monocrystalline Cu
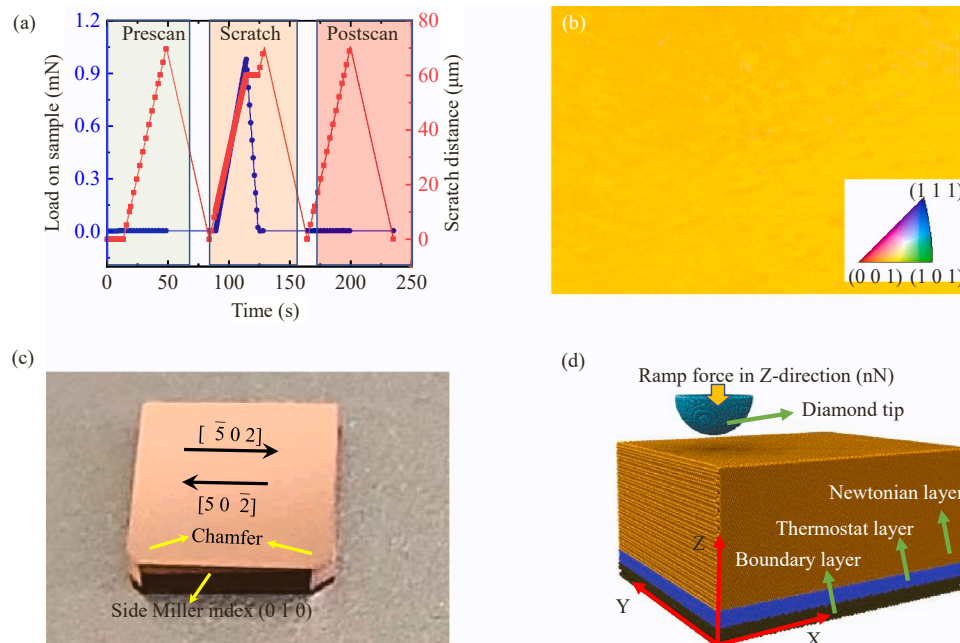


**Fig. 1.** Nano-scratching experiment and corresponding MD model along [5 0 $\overline{2}$](2 0 5) and [$\overline{5}$ 0 2](2 0 5) scratch directions under ramp force mode. (a) The changes of normal force and scratch distance with respect to time in nano-scratching. (b) The EBSD results for monocrystalline Cu specimen. (c) Schematic diagram of the scratch directions [5 0 $\overline{2}$](2 0 5) and [$\overline{5}$ 0 2](2 0 5). (d) The MD model for monocrystalline Cu and hemisphere diamond tip.

surface after the scratching process is completed. Finally, a postscan with a 2 μN constant normal force was carried out to obtain the residual scratch depth. The surface crystal orientation of the monocrystalline Cu specimen was identified by Electron Backscattered Scattering Detection (EBSD). The EBSD experiments were carried out by Scanning Electron Microscope, FEI Quanta 200 FEG, where the acceleration voltage, scan step, and the distance between the lens and the workpiece are 30 kV, 2 μm, and 12 mm, respectively. As shown in Fig. 1(b), the Miller index for monocrystalline Cu specimen surface is (2 0 5). In addition, the specimen has two chamfers which correspond to the Miller index (0 1 0) side. The scratch directions $[5\ 0\ \overline{2}](2\ 0\ 5)$ and $[\overline{5}\ 0\ 2](2\ 0\ 5)$ were determined by the (2 0 5) surface and the (0 1 0) side with chamfers, as shown in Fig. 1(c).

The grooves caused by nano-scratching were detected by Scanning Electron Microscopy (SEM) and Atomic Force Microscope (AFM). The SEM results of groove topographies was conducted by (Thermo Scientifc, Scios 2), where the acceleration voltage, current, and the distance between the lens and the workpiece are 2 kV, 0.2 nA, and 6.8 mm, respectively. Based on the commercial AFM system (Dimension Icon, Bruker, Karlsruhe, Germany), a new silicon tip (TESPA, Bruker, Karlsruhe, Germany) was used to measure the topographies of the grooves in tapping mode with a scan rate of 1 Hz. To compare the scratch and indentation hardness, the nanoindentation experiments on the (2 0 5) crystalline surface were carried out by Nano Indenter G200. The surface roughness of the monocrystalline specimen is less than 4 nm. The diamond tip in scratching process was used to conduct nano-indentation tests, and the strain rate in nano-indentation was 0.05 s$^{-1}$. The depth of nanoindentation is 300 nm. The AFM system and Nano Indenter G200 have an accuracy of less than 0.5 nm for surface morphology detection. Three nano-scratching experiments and five nano-indentation experiments were carried out to eliminate the chance of a single experimental result. In this paper, ultra-high purity single-crystal oxygen-free copper samples were used for nano-scratching and nano-indentation experiments and stored in vacuum. Since the results of multiple experiments show the same trend of change, this paper only presents the representative experimental results.

The MD simulation of the nano-scratching process was conducted by the open-source Large-scale Atomic/Molecular Massively Parallel Simulator [32]. The nano-scratching MD model contains a monocrystalline Cu workpiece and a diamond hemisphere. The workpiece with the surface Miller index (2 0 5) has a size of 40 nm × 30 nm × 20 nm, containing 2200,000 atoms. The diamond hemisphere sphere with a radius of 5 nm was set as a rigid body in nano-scratching. As shown in Fig. 1(d), the monocrystalline Cu workpiece was divided into three layers, namely the Newtonian layer, thermostat layer, and boundary layer. The boundary layer was employed to support the nano-scratching model. The atoms in the Newtonian layer would move according to Newton's law in simulation. The thermostat layer can dissipate the heat in nano-scratching. Periodic boundary condition was applied in the X and Y directions to reduce the size effect.

The MD simulation process is as follows: First, the nano-scratching model was relaxed for 50 ps under the NVT ensemble. After the MD model reached the equilibrium state, the nano-scratching process was carried out under the NPT ensemble for 30 ps. In nano-scratching, the ramp normal force from 0 to 300 nN was applied to the diamond tip in the negative Z-axis direction within a 15 nm scratch distance. The scratch speed was 20 m/s in the X-direction. Timestep and environmental temperature in the simulation are 1fs and 293 K, respectively.

The interactions among the Cu atoms were described by the EAM potential function [33,34]. The total energy $E_i$ of an atom $i$ is given by

$$E_i = F_\alpha\left(\sum_{j\neq i}\rho_\beta(r_{ij})\right) + \frac{1}{2}\sum_{j\neq i}\phi_{\alpha\beta}(r_{ij}) \tag{1}$$

Where $F$ is the embedding energy which is a function of the atomic electron density $\rho$, $\Phi$ is a pair potential interaction, and $\alpha$ and $\beta$ are the element types of atoms $i$ and $j$. The multi-body nature of the EAM potential is a result of the embedding energy term. Both summations in the formula are overall neighbors $j$ of atom $i$ within the cutoff distance.

Morse potential was employed to describe the interactions of Cu-C.

$$E = D_0\left[e^{-2\alpha(r-r_0)} - 2e^{-\alpha(r-r_0)}\right] \quad r < r_c \tag{2}$$

where $E$ the potential energy; $r$, the distance between the carbon and Cu/Al atoms; $D_0$ the binding energy, 0.087(eV); $\alpha$, the elasticity modulus 5.14(1/ Å); $r_0$, the atomic spacing; and $r_c$, the cutoff radius, 2.05(Å). Dislocations were identified and quantified with the help of the dislocation extraction algorithm (DXA) in the software OVITO [35,36].

### 2.2. Scratch and indentation hardness and COF

In this work, the effect of plastic deformation caused by scratching on the scratch hardness and COF is the main research content. Therefore, an approximate spherical indenter was selected to carry out nano-indentation and nano-scratching experiments, as shown in Fig. 2(a). Due to the magnetic properties of the cast iron tip handle, there are some differences between the SEM pictures of the tip and the actual morphology. The tip radius can be estimated from the AFM cross-section results of the scratching grooves in Fig. 3(a3) and (b3). The curvature for the diamond indenter is approximately 500 nm. In order to clarify the scratch hardness anisotropy and the relationship between indentation hardness and scratch hardness, we choose the simple definitions of nanoindentation and nano-scratching hardness that achieve the qualitative comparison of indentation hardness and scratch hardness.

The scratch hardness $H_S$ describes the link between normal force $F_N$ and projected contact area $A_S$ in nano-scratching. It can be defined as:

$$H_S = \frac{F_N}{A_S} \tag{3}$$

The lateral hardness $H_L$ can be written as:

$$H_L = \frac{F_L}{A_L} \tag{4}$$

Where the $F_L$ is the lateral force, $A_L$ is the projected contact area in the lateral direction.

The nanoindentation hardness can be written as:

$$H_I = \frac{F_N}{A_I} \tag{5}$$

Where $F_N$ is the normal force; $A_I$ is the projected contact area in nanoindentation.

For the spherical diamond indenter, as shown in Fig. 2(b), the projected contact areas $A_S$, $A_L$, and $A_I$ can be written as:

$$A_S = \frac{\pi}{2}\left(2Rh - h^2\right), A_L = \frac{2\left(2Rh - h^2\right)^{3/2}}{3R}, A_I = \pi\left(2Rh - h^2\right) \tag{6}$$

Where $R$ is the radius of the diamond indenter; $h$ is the contact depth. Here, $R$ is approximately 500 nm.

The COF is defined as:

$$\mu = \frac{F_L}{F_N} \tag{7}$$

where $F_L$ and $F_N$ is the lateral and normal force in nano-scratching, respectively.

## 3. Results and discussion

### 3.1. Surface topography and elastic recovery

As shown in Fig. 3(a), when scratching along $[\overline{5}\ 0\ 2](2\ 0\ 5)$ direction, the chip appears in front of the groove under the ramp normal force
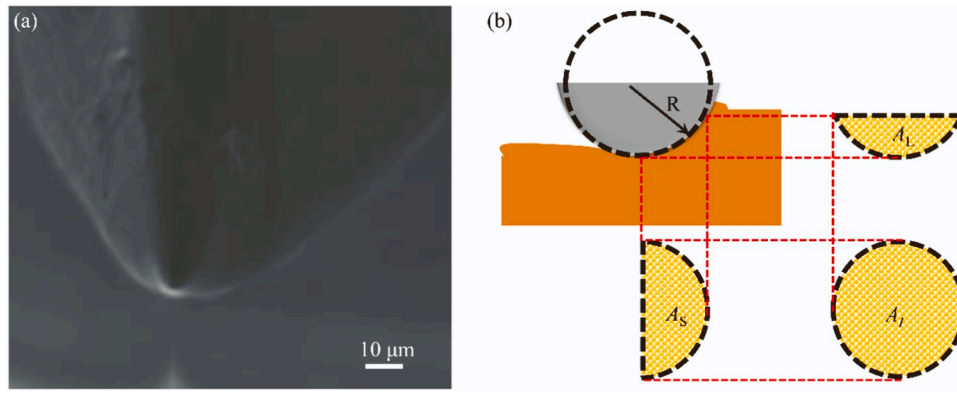
**Fig. 2.** (a) SEM image for the diamond tip. (b) Schematic diagram of projected contact areas $A_S$, $A_L$, and $A_I$.
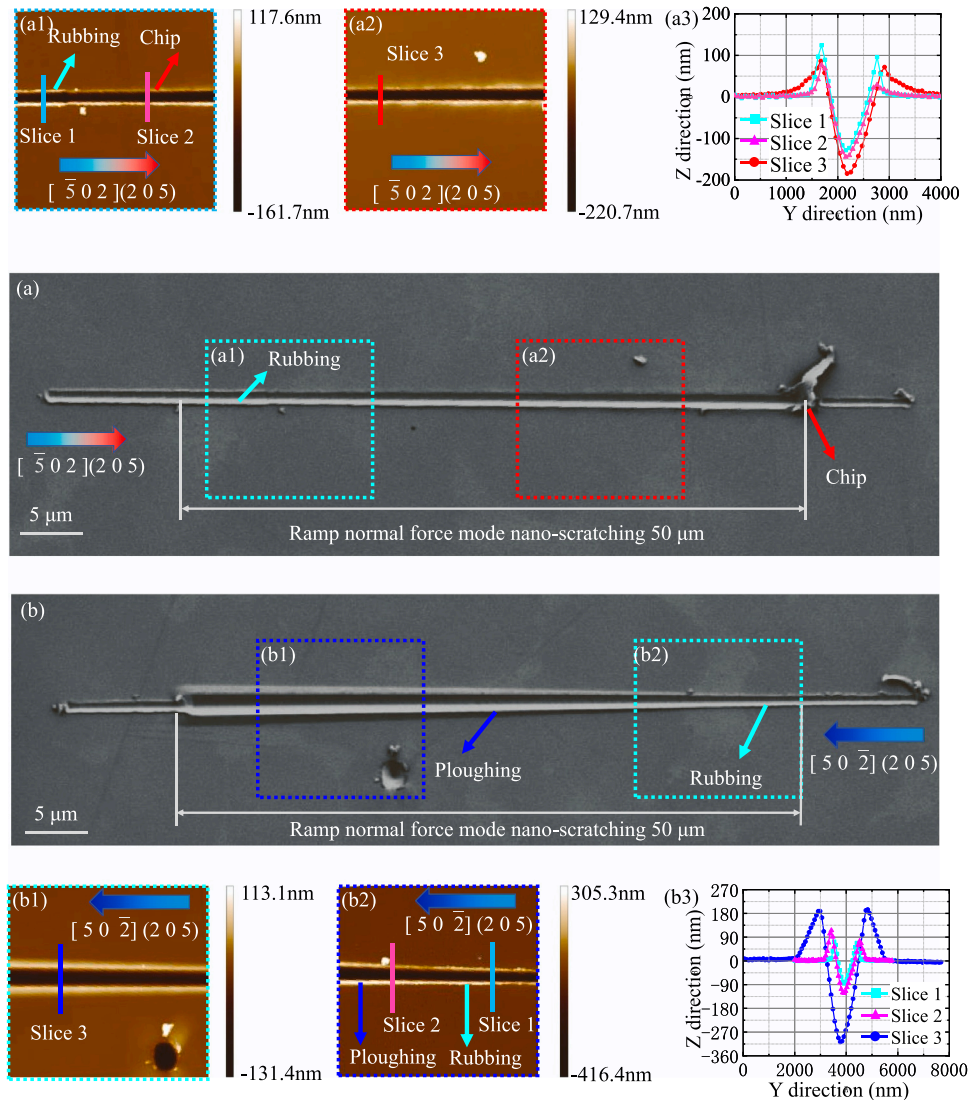


**Fig. 3.** The surface topography for scratching on (2 0 5) plane. (a) and (b) SEM results for grooves along $[\bar{5}\ 0\ 2](2\ 0\ 5)$ and $[5\ 0\ \bar{2}](2\ 0\ 5)$, respectively. (a1)-(a2) and (b1)-(b2) AFM scan results for the partial groove in Fig. 3(a) and (b), respectively. (a3) and (b3) Groove morphologies of different cross-sections in Fig. 3(a1)-(a2) and (b1)-(b2), respectively.

model. The rubbing dominates the scratch process under a small scratch depth. As the scratch depth increases, the monocrystalline Cu scratch behavior changes from rubbing to chip formation, thereby forming the chip in front of the groove. The AFM results in Fig. 3(a1)-(a3) indicate

that the pile-up on both sides of the groove under the rubbing stage is higher than that under the chip formation stage. The SEM result in Fig. 3 (a) is equivalent to photos, which do not include quantitative information on surface height. The AFM results in Fig. 3 (a1)-(a3) are the true

pile-up height. Slice 1 in Fig. 3(a1) is a typical cross-section in the rubbing stage. As shown in Fig. 3(a3), the groove depth and pile-up on both sides of the groove of slice 1 are 130 nm and 110 nm, respectively. For the stage of chip formation, the groove depth for the typical cross-section slices 2 and 3 are 150 nm and 185 nm, respectively, which are larger than that for slice 1. However, the pile-up heights for slices 2 and 3 are less than that of slice 1.

Fig. 3(b) shows the nano-scratching result for scratching along $[5\ 0\ \overline{2}](2\ 0\ 5)$ direction. It can be found that no chip removal occurred during the entire nano-scratching process. Similar to the scratch direction $[\overline{5}\ 0\ 2](2\ 0\ 5)$, the rubbing dominates the scratch process under a small scratch depth. As the scratch depth increases, the monocrystalline Cu scratch behavior changes from rubbing to ploughing, thereby forming the obvious pile-up on both sides of the groove. As shown in Fig. 3 (b2), for the rubbing stage, the pile-up on both sides of the groove is not smooth, showing a burrs shape. However, for the ploughing stage, the size of the pile-up on both sides of the groove is larger and smoother, as shown in Fig. 3(b1). Fig. 3(b3) shows the typical groove cross-sections for scratching along $[5\ 0\ \overline{2}](2\ 0\ 5)$ direction. It can be found that the scratch depth and pile-up on both sides of the groove both increase with the normal force. Fig. 3(b3) shows that the scratch depth for slices 1, 2, and 3 are approximately 90 nm, 130 nm, and 300 nm, respectively. And the pile-up on both sides of the grooves for slices 1, 2, and 3 are approximately 80 nm, 120 nm, and 210 nm, respectively. The chips at starting parts of grooves in Fig. 3(a) and (b) are formed in post scanning stage.

The nano scratching experiments can only obtain the final experimental results, making it difficult to observe the transformation process of rubbing and chip. To further clarify the variation of monocrystalline Cu scratching behavior with respect to scratch depth, the MD simulations for scratching monocrystalline Cu along the $[\overline{5}\ 0\ 2](2\ 0\ 5)$ and $[5\ 0\ \overline{2}](2\ 0\ 5)$ directions under ramp loading were conducted. Fig. 4 shows the MD simulation results for the variation of scratching behavior with scratch depth along $[\overline{5}\ 0\ 2](2\ 0\ 5)$ and $[5\ 0\ \overline{2}](2\ 0\ 5)$ directions. As shown in Fig. 4(a1)-(a3), for the scratch direction $[\overline{5}\ 0\ 2](2\ 0\ 5)$, the pile-up caused by scratching exhibits a semicircular distribution when the scratch depth is less than 0.4 nm. In this case, the rubbing behavior dominates the scratching process. With the scratch depth increasing, the pile-up in front of the groove gradually becomes a triangular chip, as shown in Fig. 4(a4)-(a6). In this case, the $< 1\ 1\ 0 >\ \{1\ 1\ 1\}$ slip systems

was activated, resulting in a triangular material pile-up on the specimen surface in nano-scratching [30,31], and the chip removal state dominates the scratching process. For the scratch direction $[5\ 0\ \overline{2}](2\ 0\ 5)$, the pile-up caused by scratching exhibits a semicircular distribution under the scratch depth of 0.2 nm in rubbing stage, as shown in Fig. 4(b1). When the scratch depth are 0.35 nm and 0.4 nm, as shown in Fig. 4 (b2)-(b3), a distinct triangular pile-up caused by the activated $< 1\ 1\ 0 >$ $\{1\ 1\ 1\}$ slip system appears on one side of the groove, which indicates that the scratching behavior for the scratch direction $[5\ 0\ \overline{2}](2\ 0\ 5)$ is changing from rubbing to ploughing. As the scratch depth increases, the ploughing pile-up appears on both sides of the groove and significantly increases with the load. However, in the rubbing stage, the pile-up on both sides of the groove does not increase significantly with the load increase, which is the important difference between the ploughing and rubbing stages. The MD simulation results for $[\overline{5}\ 0\ 2](2\ 0\ 5)$ and $[5\ 0\ \overline{2}](2\ 0\ 5)$ scratch directions agree well with the nano-scratching experimental results in Fig. 3.

According to the nano scratching results in Figs. 3 and 4, the scratching behavior of monocrystalline Cu varies significantly with the scratch depth and scratch direction. For the nano-scratching process under the ramp normal force model, when the scratch depth is too small to activate the $< 110 >\ \{111\}$ slip systems, the nano-scratching process for monocrystalline Cu will be dominated by rubbing. On the contrary, under larger scratch depth, the $< 110 >\ \{111\}$ slip systems will be activated and dominate the scratching behavior of monocrystalline Cu, namely ploughing or chip removal.

Moreover, when scratching along $[\overline{5}\ 0\ 2](2\ 0\ 5)$ and $[5\ 0\ \overline{2}](2\ 0\ 5)$ directions, there are also significant differences in elastic recovery and scratch depth. As shown in Fig. 5(a), the ramp normal force ranging from 0 to 1 mN corresponds to the scratch distance ranging from 0 to 50 μm. The maximum scratch depth for $[\overline{5}\ 0\ 2](2\ 0\ 5)$ and $[5\ 0\ \overline{2}](2\ 0\ 5)$ directions are approximately 190 nm and 310 nm, respectively. Meanwhile, for the $[5\ 0\ \overline{2}](2\ 0\ 5)$ scratch direction, the scratch and residual depth increase linearly when the normal force increases. For the $[\overline{5}\ 0\ 2]$ $(2\ 0\ 5)$ scratch direction, the scratch and residual depth increase linearly in the initial stage of nano-scratching. However, as the normal force increases, the scratch and residual depth fluctuate, and the increment shows a decreasing trend. The MD simulation results in Fig. 5(b) also show the difference in scratch depth when scratching along $[\overline{5}\ 0\ 2](2\ 0\ 5)$ and $[5\ 0\ \overline{2}](2\ 0\ 5)$ directions. Fig. 5(c) and (d) show the elastic
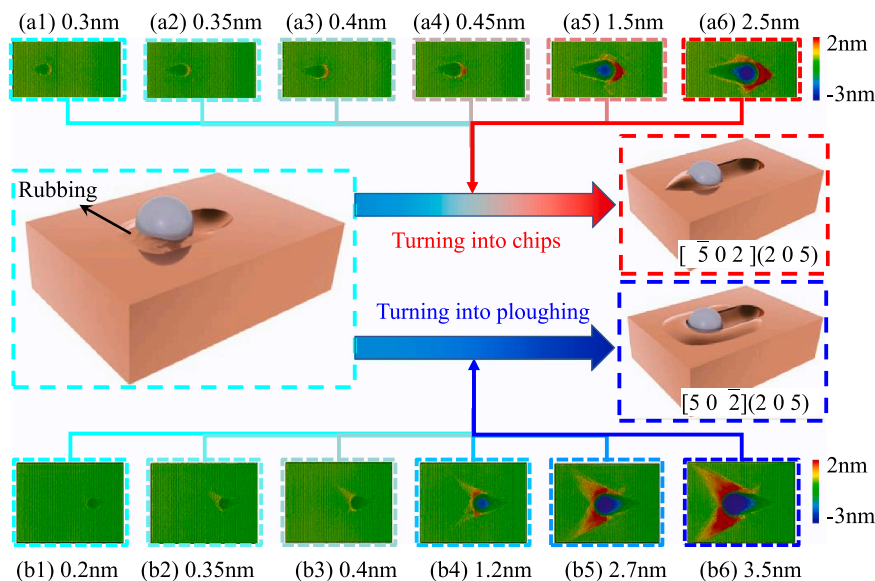


**Fig. 4.** The transformation of scratching behaviors under ramp normal force. (a1)-(a6) and (b1)-(b6) are the surface topography for $[\overline{5}\ 0\ 2](2\ 0\ 5)$ and $[5\ 0\ \overline{2}](2\ 0\ 5)$ scratch directions under different scratch depth, respectively. The Cu atoms were colored by height.
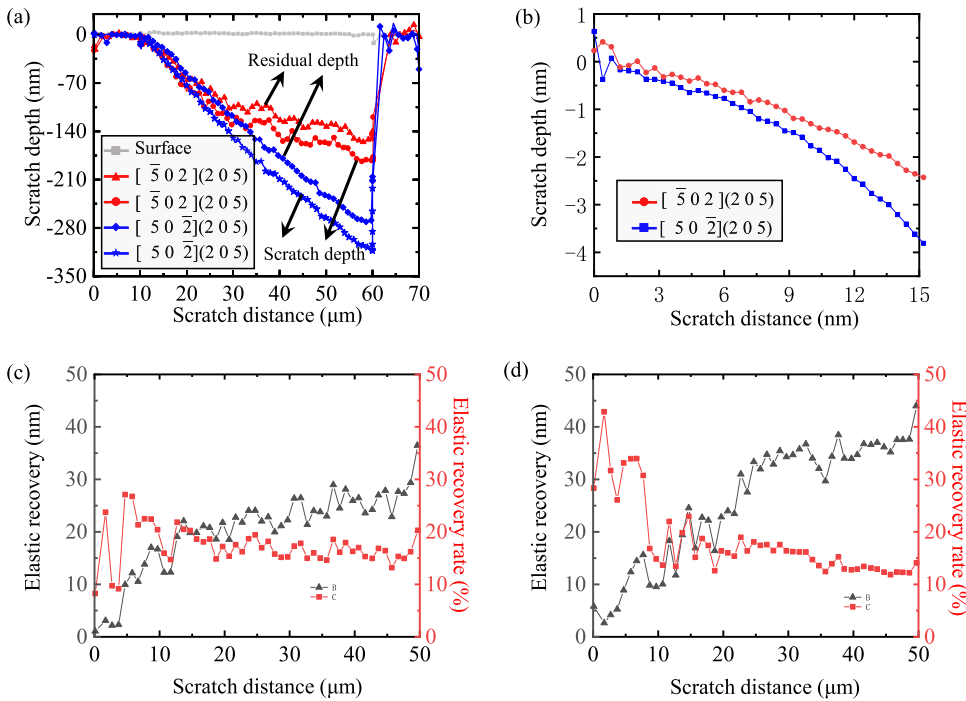
**Fig. 5.** (a) scratch and residual depth for scratching along $[\overline{5}\,0\,2](2\,0\,5)$ and $[5\,0\,\overline{2}](2\,0\,5)$ directions. (b) The scratch depth obtained by MD simulations for $[\overline{5}\,0\,2](2\,0\,5)$ and $[5\,0\,\overline{2}](2\,0\,5)$ scratch directions. (c) The elastic recovery and elastic recovery rate for $[\overline{5}\,0\,2](2\,0\,5)$ scratch directions. (d) The elastic recovery and elastic recovery rate for $[5\,0\,\overline{2}](2\,0\,5)$ scratch directions, where the elastic recovery rate is the ratio of the difference between the scratch depth and the residual depth, and the elastic recovery rate is the ratio of the difference between the scratch depth and the residual depth to the residual depth.

recovery and elastic recovery rate for scratching along $[\overline{5}\,0\,2](2\,0\,5)$ and $[5\,0\,\overline{2}](2\,0\,5)$ directions. It can be found that the elastic recovery increases as the scratch distance or depth increases along $[\overline{5}\,0\,2](2\,0\,5)$ and $[5\,0\,\overline{2}](2\,0\,5)$ directions. The elastic recovery for $[5\,0\,\overline{2}](2\,0\,5)$

scratch direction is larger than that of $[\overline{5}\,0\,2](2\,0\,5)$ scratch direction. The elastic recovery rate for $[5\,0\,\overline{2}](2\,0\,5)$ scratch direction decreases as the scratch distance or depth increases, from 40% to 15%. Whereas, for the $[\overline{5}\,0\,2](2\,0\,5)$ scratch direction, the elastic recovery rate slightly
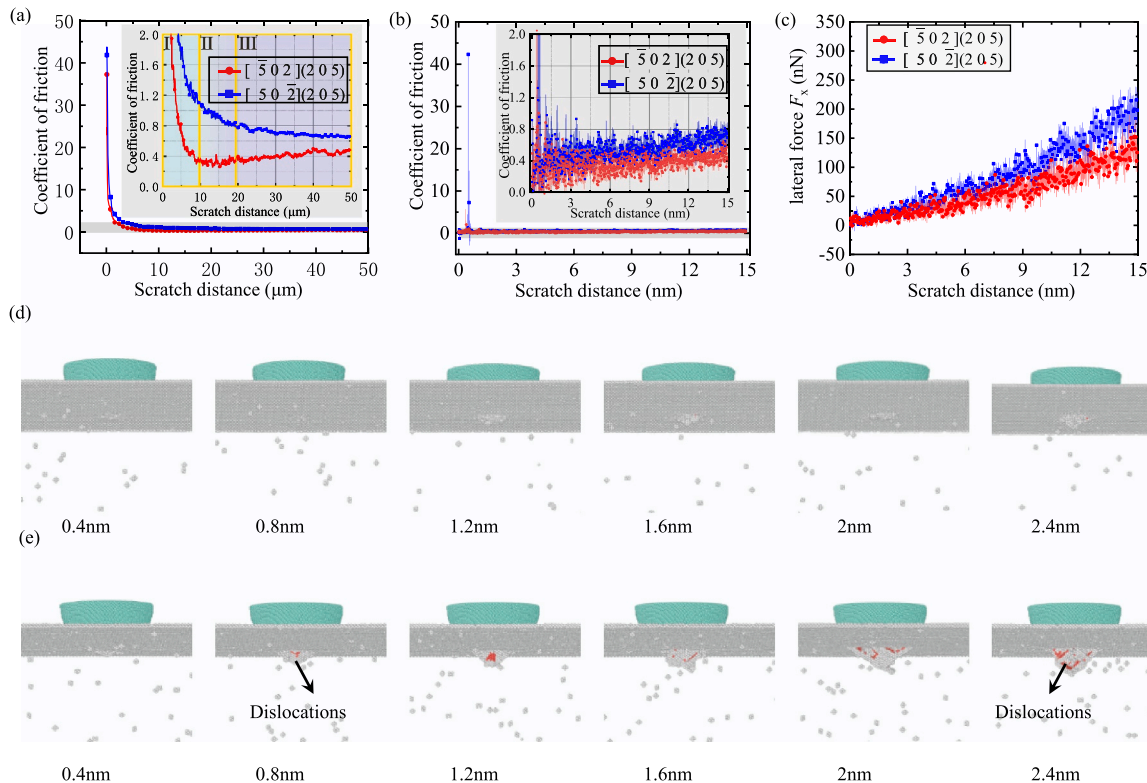


**Fig. 6.** The change of COF with respect to scratching distance obtained by nano-scratching experiments and MD simulations under $[\overline{5}\,0\,2](2\,0\,5)$ and $[5\,0\,\overline{2}](2\,0\,5)$ scratch directions, respectively. (a) and (b)The change of COF with respect to scratching distance obtained by nano-scratching experiments and MD simulation, respectively, and the inset with an enlarged view of the COF in the range 0–2. (c) The normal and lateral force in MD simulation for $[\overline{5}\,0\,2](2\,0\,5)$ and $[5\,0\,\overline{2}](2\,0\,5)$ scratch directions. (d) and (e) the subsurface defect caused by scratching in the rubbing stage along $[\overline{5}\,0\,2](2\,0\,5)$ and $[5\,0\,\overline{2}](2\,0\,5)$ scratch directions, respectively.

decreases as the scratch distance or depth increases, from 28% to 18%. In addition, as shown in Fig. 5(a), when the scratch distance is less than 10 μm, the variation of scratch depth with respect to scratch distance is similar under $[\bar{5}\,0\,2](2\,0\,5)$ and $[5\,0\,\bar{2}](2\,0\,5)$ directions. In this case, the scratching behaviors under $[\bar{5}\,0\,2](2\,0\,5)$ and $[5\,0\,\bar{2}](2\,0\,5)$ directions are both rubbing.

### 3.2. Coefficient of friction

The nano scratching results in Figs. 3 and 4 show significant changes in scratching behavior with respect to scratch direction and scratch depth. The COF under different scratching behaviors should be different. Fig. 6(a) shows the variation of COF with respect to scratch distance when scratching along $[\bar{5}\,0\,2](2\,0\,5)$ and $[5\,0\,\bar{2}](2\,0\,5)$ directions. The COF is as high as 35–45 in the initial stage of nano-scratching and tends to stabilize as the scratch distance increases. The stable COFs for $[\bar{5}\,0\,2](2\,0\,5)$ and $[5\,0\,\bar{2}](2\,0\,5)$ scratch directions are approximately 0.5 and 0.7, respectively. The variation of COF with the scratch depth and scratch direction is caused by the change in scratching behavior, and the scratching results in Figs. 3 and 4 are the corresponding physical evidence. Therefore, combining the changes in scratching behavior and COF, Fig. 6(a) can be divided into three parts, namely rubbing stage (part I), transformation stage (part II), and ploughing or chip stage (part III). For part I, the nano-scratching behaviors for $[\bar{5}\,0\,2](2\,0\,5)$ and $[5\,0\,\bar{2}](2\,0\,5)$ scratch directions are both rubbing, as shown in Fig. 3. The COF in part I decreases drastically as the scratch distance increases. Combining the nano scratching results in Figs. 3 and 4, it can be found that the plastic deformation mode of monocrystalline Cu materials in rubbing initial stage is that the Cu atoms irregularly pile up on the surface, which requires a relatively large lateral force, resulting in a higher COF. As the scratch depth increases, the normal force significantly increases, resulting that the COF sharply decreases as the scratch depth or distance increases. Meanwhile, the decrease in COF is more obvious when scratching along $[\bar{5}\,0\,2](2\,0\,5)$ direction. For part II, the scratch behavior for $[5\,0\,\bar{2}](2\,0\,5)$ direction is changing from rubbing to ploughing. The COF in part II decreases as the scratch distance increases. The scratch behavior for $[\bar{5}\,0\,2](2\,0\,5)$ scratch direction is changing from rubbing to chip removal in part II, and the COF is stable. In part III, the nano-scratching process is dominated by ploughing along $[5\,0\,\bar{2}](2\,0\,5)$ direction, and the COF tends to stabilize. However, under the chip stage in part III, the COF along $[5\,0\,\bar{2}](2\,0\,5)$ direction increases as the scratch distance increases slightly. It can be found that when scratching along $[\bar{5}\,0\,2]$ $(2\,0\,5)$ and $[5\,0\,\bar{2}](2\,0\,5)$ directions, the change of COF with respect to scratch distance is different under the same normal force. The main reason is that, as increasing normal force, the scratching behavior for $[\bar{5}\,0\,2](2\,0\,5)$ direction changes from rubbing to chip, while the scratching behavior for $[5\,0\,\bar{2}](2\,0\,5)$ direction changes from rubbing to ploughing, for detailed analysis, refer to Section 3.4.

To further clarify the correlation between the variation of COF and scratch behavior, Fig. 6(b) shows the variation of COF with the scratch distance obtained by MD simulations. It can be observed that the MD simulation results of COF have a similar trend to the nano scratching experimental results in Fig. 6(a), which indicates that the COF is closely related to the scratching behavior. In the initial stage of scratching, the COF obtained by MD simulations along $[5\,0\,\bar{2}](2\,0\,5)$ scratch direction is as high as 43, which is similar to nano-scratching experimental results in Fig. 6(a). As the scratch distance increases, the COF for $[\bar{5}\,0\,2](2\,0\,5)$ and $[5\,0\,\bar{2}](2\,0\,5)$ scratch directions both show a decreasing trend and finally stabilize at 0.5 and 0.7, respectively. The results of the MD simulation agree well with that of nano-scratching experiments. Fig. 6 (c) shows the change of lateral force in the X-direction with respect to scratch distance for $[\bar{5}\,0\,2](2\,0\,5)$ and $[5\,0\,\bar{2}](2\,0\,5)$ directions. During the nano-scratching process, the lateral force $F_x$ for $[5\,0\,\bar{2}](2\,0\,5)$ scratch direction is larger than that for $[\bar{5}\,0\,2](2\,0\,5)$ scratch direction. In addition, as shown in Fig. 6(a) and (b), the COFs for the rubbing stage are different when scratching along $[\bar{5}\,0\,2](2\,0\,5)$ and $[5\,0\,\bar{2}](2\,0\,5)$ directions. The MD simulation results for the rubbing stage along $[\bar{5}\,0\,2](2\,0\,5)$ and $[5\,0\,\bar{2}](2\,0\,5)$ scratch directions are shown in Fig. 6(d) and (e), respectively. It can be found that, under $[\bar{5}\,0\,2](2\,0\,5)$ and $[5\,0\,\bar{2}](2\,0\,5)$ scratch directions, the subsurface defect caused by scratching is different. Hexagonal close-packed (HCP) dislocations are generated when scratching along $[5\,0\,\bar{2}](2\,0\,5)$ direction. However, for $[\bar{5}\,0\,2](2\,0\,5)$ scratch direction, HCP dislocations do not appear on the subsurface. The HCP dislocation structure for $[5\,0\,\bar{2}](2\,0\,5)$ scratch direction will strengthen the monocrystalline material, resulting in a larger lateral force $F_x$ and COF during the nano-scratching process.

### 3.3. Scratch hardness and lateral hardness

During the nano scratching process under ramp normal force, similar to the COF, the scratch hardness also changes with the scratch depth and direction. The change in scratch hardness with respect to scratch distance is shown in Fig. 7(a). Combining the variations of scratching behaviors and COF with the scratch distance in Sections 3.1 and 3.2, the nano-scratching processes for $[\bar{5}\,0\,2](2\,0\,5)$ and $[5\,0\,\bar{2}](2\,0\,5)$ scratch directions can be divided into three stages according to the change in scratch hardness, namely, rubbing stage, transform stage, and chip or ploughing stage. As shown in Fig. 3, when the scratch distance is less than 10 μm, the nano-scratching processes along $[\bar{5}\,0\,2](2\,0\,5)$ and $[5\,0\,\bar{2}](2\,0\,5)$ scratch directions are both dominated by rubbing in scratching stage I. In this case, the scratch hardness for $[\bar{5}\,0\,2](2\,0\,5)$ and $[5\,0\,\bar{2}](2\,0\,5)$ directions shows a decreasing trend as the scratch distance increases. Meanwhile, due to the strengthening effect of dislocations in Fig. 6(d) and (e), the scratch hardness for $[5\,0\,\bar{2}](2\,0\,5)$ direction is slightly larger than that for $[\bar{5}\,0\,2](2\,0\,5)$ direction. In general, the scratch hardness for $[\bar{5}\,0\,2](2\,0\,5)$ and $[5\,0\,\bar{2}](2\,0\,5)$ directions are similar in the scratching stage I, namely, the rubbing stage. In scratching stage II, the plastic deformation behavior along $[\bar{5}\,0\,2](2\,0\,5)$ scratch direction starts to change from rubbing to chip, and the scratch hardness increases as the scratch distance increases. Similarly, for $[5\,0\,\bar{2}](2\,0\,5)$ scratch direction, the scratch behavior starts to change from rubbing to ploughing, and the scratch hardness also increases as the scratch distance increases. Compared with stage I, the scratch hardness for $[5\,0\,\bar{2}](2\,0\,5)$ direction is slightly less than that for $[\bar{5}\,0\,2](2\,0\,5)$ direction in stage II, namely, the transitional stage of scratch behaviors. In scratch stage III, the scratch behavior for $[\bar{5}\,0\,2](2\,0\,5)$ and $[5\,0\,\bar{2}](2\,0\,5)$ directions are chip removal and ploughing, respectively. And the increasing trend of scratch hardness with respect to the increasing scratch distance along $[5\,0\,\bar{2}](2\,0\,5)$ direction is more obvious than that along $[\bar{5}\,0\,2](2\,0\,5)$ direction. It can be found that the change in scratch hardness is closely related to the plastic deformation behavior caused by scratching when scratching along $[\bar{5}\,0\,2](2\,0\,5)$ and $[5\,0\,\bar{2}](2\,0\,5)$ directions. Tsybenko et al. [12] also found that the scratch hardness first decreases and then increases with the increase of normal load.

Fig. 7(b) shows the changes in scratch hardness and indentation hardness with respect to scratch depth. Referring to Fig. 5(a), when the scratch depth is less than 75 nm, the scratch behaviors for $[\bar{5}\,0\,2](2\,0\,5)$ and $[5\,0\,\bar{2}](2\,0\,5)$ directions are mainly rubbing. In this case, the indentation hardness is similar to the scratch hardness along $[\bar{5}\,0\,2](2\,0\,5)$ and $[5\,0\,\bar{2}](2\,0\,5)$ scratch directions. And the scratch and indentation hardness decrease as the scratch depth increases. However, when the scratch depth is larger than 75 nm, referring to Fig. 5(a), the scratch behaviors for $[\bar{5}\,0\,2](2\,0\,5)$ and $[5\,0\,\bar{2}](2\,0\,5)$ directions are chip and ploughing, respectively. In this case, the scratch hardness is larger than the indentation hardness and increases as the scratch depth increases. The change of lateral hardness with respect to scratch distance in the nano-scratching process along $[\bar{5}\,0\,2](2\,0\,5)$ and $[5\,0\,\bar{2}](2\,0\,5)$ scratch
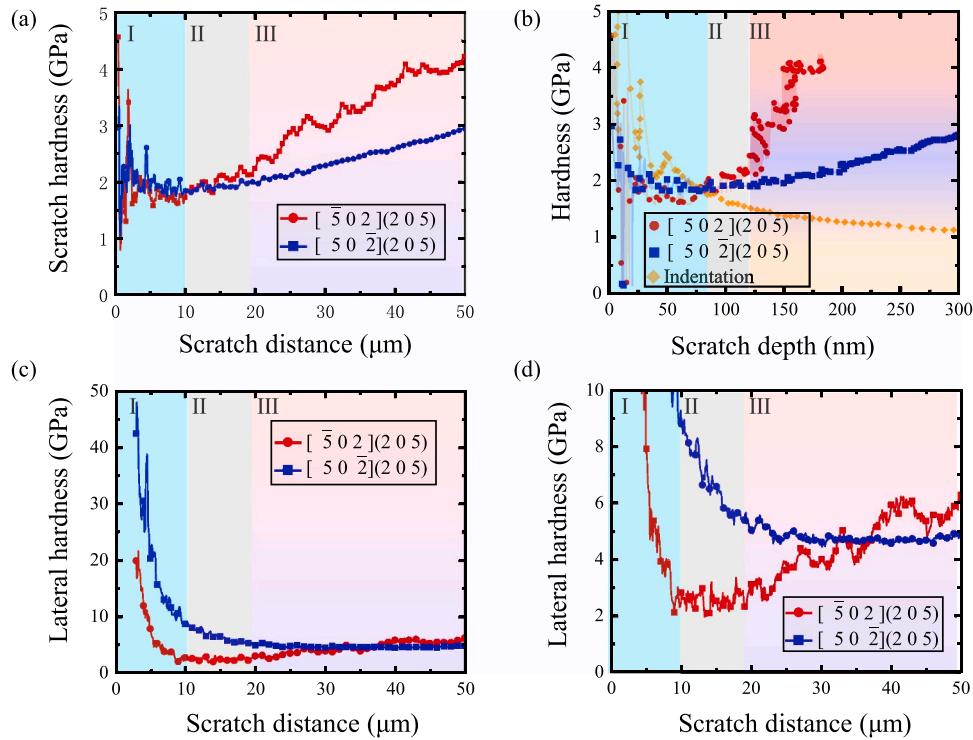
**Fig. 7.** Changes in the mechanical properties of monocrystalline Cu materials in nano-scratching. (a) and (b) The change of scratch hardness with respect to scratch distance and scratch depth, respectively. (c) The change of lateral hardness with respect to scratch distance, where (d) is a partial magnification of (c).

directions are shown in Fig. 7(c) and (d). In the scratching stage I, namely the rubbing stage, the lateral hardness decreases as the scratch distance increases when scratching along $[\bar{5}\,0\,2](2\,0\,5)$ and $[5\,0\,\bar{2}]$ directions. In this stage, the lateral hardness of $[\bar{5}\,0\,2](2\,0\,5)$ scratch directions is larger than that of $[5\,0\,\bar{2}](2\,0\,5)$ scratch directions. For the scratching stage II, the lateral hardness for $[5\,0\,\bar{2}](2\,0\,5)$ scratch directions tends to stabilize with the scratch behavior changing from rubbing to ploughing. In scratching stage III, the lateral hardness for $[5\,0\,\bar{2}](2\,0\,5)$ direction is stable at 5 GPa. However, the lateral hardness along $[\bar{5}\,0\,2](2\,0\,5)$ scratch directions increases as the scratch distance increases in scratching stages II and III, namely, rubbing-to-chip

transition and chip removal stages.

*3.4. Analyzing the difference of scratching behaviors and mechanical properties in rubbing, chip, and ploughing stages*

The results of nano-scratching experiments and corresponding MD simulation show that, under the same normal force and scratch speeds, the scratch depth, scratch hardness, COF, and scratching behaviors are all different when scratching along $[\bar{5}\,0\,2](2\,0\,5)$ and $[5\,0\,\bar{2}](2\,0\,5)$ directions. For the rubbing stage, the COF and scratch hardness are larger than that of chip formation and ploughing, and decrease as the
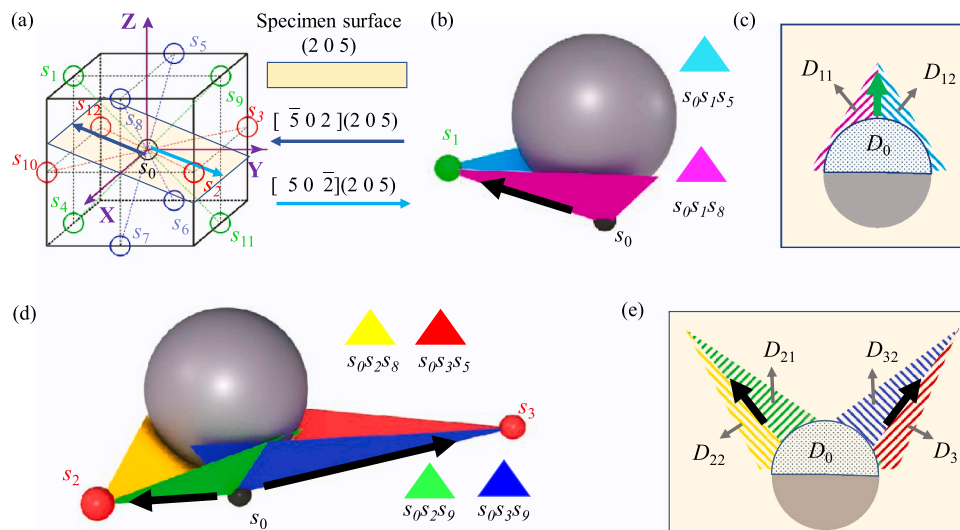


**Fig. 8.** The scratching deformation mechanism for $[\bar{5}\,0\,2](2\,0\,5)$ and $[5\,0\,\bar{2}](2\,0\,5)$ directions in chip formation and ploughing stages. (a) The specimen surface and scratch directions in crystalline reference; (b) The slip direction $s_0s_1$ and corresponding slip planes; (c) The surface pile-up for scratching along $[\bar{5}\,0\,2](2\,0\,5)$ direction; (d) The slip directions $s_0s_2$ and $s_0s_3$, and corresponding slip planes; (e) The surface pile-up for scratching along $[5\,0\,\bar{2}](2\,0\,5)$ direction.

scratch depth increases. Meanwhile, the $< 1\,1\,0 > \{1\,1\,1\}$ slip system was not activated in the rubbing stage, resulting in a semicircular pile-up distribution on surface. During the chip formation and ploughing stages, the $< 1\,1\,0 > \{1\,1\,1\}$ slip systems was activated, and the chip formation stage shows a larger scratching hardness and smaller COF than ploughing stage. The difference in scratch depth, COF, and scratch hardness between the chip formation and ploughing stages can be effectively analyzed through the difference in scratch behavior caused by the activated $< 1\,1\,0 > \{1\,1\,1\}$ slip system during the nano scratching process. The specific process is as follows:

As shown in Fig. 8(a), when scratching along $[\bar{5}\,0\,2](2\,0\,5)$ direction, the $[1\,\bar{1}\,0]$ slip direction $s_0 s_1$ will be activated, and the number of slip atoms is determined by the slip planes $s_0 s_1 s_8$ and $s_0 s_1 s_5$, which are tangent to the scratching tip, as shown in Fig. 8(b). In this case, the pile-up on the specimen surface will be as shown in areas $D_{11}$ and $D_{12}$ in Fig. 8(c), which are the projection of planes $s_0 s_1 s_8$ and $s_0 s_1 s_5$ on the specimen surface, respectively. Since the pile-up is mainly concentrated in front of the tip, the chip formation dominates the scratching process. Similarly, when scratching along $[5\,0\,\bar{2}](2\,0\,5)$ direction, as shown in Fig. 8(a) and (d), the slip directions $s_0 s_2$ and $s_0 s_3$ will be activated in nano-scratching, and the pile-up on the specimen surface will be as shown in areas $D_{21}$, $D_{22}$, $D_{31}$, and $D_{32}$ in Fig. 8(e). In this case, the ploughing pile-up dominates the scratching process. The results of MD simulation in Fig. 4(a4)-(a6) and (b4)-(b6) and our previous work [30, 31] can support the above analysis process.

For the scratch direction $[\bar{5}\,0\,2](2\,0\,5)$, it should be noted that the atomic slip direction $s_0 s_1$ in Fig. 8(a)-(b) and Fig. 9(a) is towards the specimen surface, and the $D_0$ part of the diamond tip in Fig. 8(c) and (e) will hinder the slip motion of some Cu atoms. Therefore, due to the activated $< 1\,1\,0 > \{1\,1\,1\}$ slip system, the $D_0$ part of the tip will be subjected to a force, whose upward component in the Z direction is defined as the atomic slip resistance $F_{slip}$ in nano scratching, as shown in Fig. 9(a). The atomic slip resistance $F_{slip}$ is closely related to the anisotropy and size effect of scratch hardness and COF in nano scratching. At present, giving a quantitative expression for atomic slip resistance $F_{slip}$ is a difficult challenge. Here, we only quantitatively discuss the anisotropy of scratch hardness and COF based on the

properties of atomic slip resistance $F_{slip}$. The specific analysis for the difference in atomic slip resistance $F_{slip}$ along $[5\,0\,\bar{2}](2\,0\,5)$ and $[\bar{5}\,0\,2](2\,0\,5)$ scratch directions is as follows. As shown in Fig. 9(b), when scratching along $[\bar{5}\,0\,2](2\,0\,5)$ direction, the atomic slip resistance $F_{slip}$ will increase with the $\cos\varphi_1$, where $\varphi_1$ is the angle between the slip direction $s_0 s_1$ and the workpiece surface normal vector. Equivalently, the projections ratio for $D_0/(D_{11} + D_{12})$ and $D_0/(D_{21} + D_{22} + D_{31} + D_{32})$ on the specimen surface can also describe the relative magnitude for the atomic slip resistance $F_{slip}$ between the chip removal and ploughing stage. During the nano-scratching process, the Cu atoms inside the workpiece move towards the specimen surface along the corresponding $\{1\,1\,1\}$ slip plane, resulting in chip removal and ploughing phenomena, as shown in Fig. 8(b) and (d). The workpiece surface material pile-up formed by the atoms moving towards the workpiece surface in chip removal and ploughing stages are shown in Fig. 8(c) and (e), respectively. It can be found that, compared with the chip removal stage, the material pile-up area on the workpiece surface in ploughing stage is larger, so the $D_0$ part in front of the diamond tip has a smaller hindrance effect on the movement of atoms toward the workpiece surface, resulting in a relatively small atomic slip resistance $F_{slip}$.

According to the difference in atomic slip resistance $F_{slip}$ along the $[5\,0\,\bar{2}](2\,0\,5)$ and $[\bar{5}\,0\,2](2\,0\,5)$ scratch directions, the difference in scratch depth, COF, and scratch hardness under the chip formation and ploughing stages can be explained as follows. The directions for the atomic slip resistance $F_{slip}$ and the indentation force $F_N$ force is opposite, resulting in a decrease in the effective normal force $F_{ef}$. As shown in Fig. 8(c) and (e), due to the ratio of $D_0/(D_{11} + D_{12})$ larger than that of $D_0/(D_{21} + D_{22} + D_{31} + D_{32})$, the atomic slip resistance $F_{slip}$ for the chip formation direction $[\bar{5}\,0\,2](2\,0\,5)$ will be larger than that for the ploughing direction $[5\,0\,\bar{2}](2\,0\,5)$ in nano-scratching. Therefore, as shown in Fig. 5(a), the scratch depth along $[\bar{5}\,0\,2](2\,0\,5)$ direction will be less than that along $[5\,0\,\bar{2}](2\,0\,5)$ direction under the same normal load when the scratch distance is larger than 10 μm. Meanwhile, according to Eq. (3), the scratch hardness will increase as the scratch depth decreases under a certain normal force $F_N$; therefore, the scratch hardness for the chip formation direction $[\bar{5}\,0\,2](2\,0\,5)$ is larger than that for
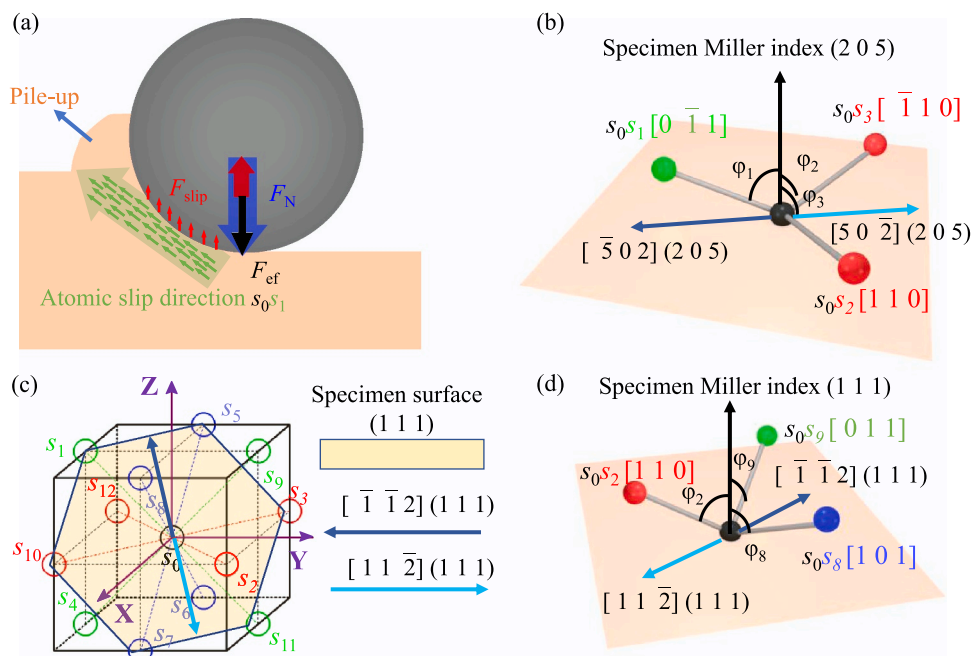


**Fig. 9.** Schematic diagram for analyzing the anisotropy of mechanical properties in monocrystalline Cu nano scratching process based on slip resistance. (a) The atomic slip resistance $F_{slip}$ during the nano-scratching process. (b) The spatial positional relationship between atomic slip direction and scratch direction $[\bar{5}\,0\,2](2\,0\,5)$ and $[5\,0\,\bar{2}](2\,0\,5)$. (c) and (d) The spatial positional relationship between atomic slip direction and scratch direction $[\bar{1}\,\bar{1}\,2](1\,1\,1)$ and $[1\,1\,\bar{2}](1\,1\,1)$.

the ploughing direction $[5\ 0\ \overline{2}](2\ 0\ 5)$, as shown in the stages II and III in Fig. 7(a). Due to the atomic slip resistance $F_{slip}$, the indentation hardness is less than the scratch hardness, as shown in Fig. 7(b). In addition, Brookes et al. [16] conducted the scratching experiments along $[1\ 1\ \overline{2}]$ and $[\overline{1}\ \overline{1}\ 2]$ directions on monocrystalline Cu (1 1 1) surface. Experimental results show that the ratio of scratch hardness to indentation hardness for $[1\ 1\ \overline{2}](1\ 1\ 1)$ and $[\overline{1}\ \overline{1}\ 2](1\ 1\ 1)$ scratch directions are 1.71 and 1.03, respectively. The experimental results for Brookes et al. can be explained by the property of the atomic slip resistance $F_{slip}$. As shown in Fig. 9(c) and (d), when scratching along $[\overline{1}\ \overline{1}\ 2](1\ 1\ 1)$ direction, the slip direction $s_0s_2$ will be activated. However, when scratching along $[1\ 1\ \overline{2}](1\ 1\ 1)$, direction the slip directions $s_0s_8$ and $s_0s_9$ will be activated. Similar to the scratch hardness analysis for scratch directions $[5\ 0\ \overline{2}](2\ 0\ 5)$ and $[\overline{5}\ 0\ 2](2\ 0\ 5)$, the scratch hardness for $[1\ 1\ \overline{2}](1\ 1\ 1)$ direction will be larger than that for $[\overline{1}\ \overline{1}\ 2](1\ 1\ 1)$ scratch direction. In addition, the COF mainly depends on the magnitude of the lateral force $F_L$ under the same normal force, as shown in Eq. (7). The effective normal force $F_{ef}$ in chip formation stage is smaller than that in the ploughing stage under the same normal force, resulting in smaller scratch depth and the lateral force $F_L$. Therefore, the friction coefficient during the chip formation stage is smaller than that during the ploughing stage.

In addition, for the rubbing stage, the $< 1\ 1\ 0 > \{1\ 1\ 1\}$ slip system was not activated; therefore, there is no atomic slip resistance, and the effective normal force $F_{ef}$ is equal to normal force $F_N$. In this case, the scratch depth for scratch directions $[\overline{5}\ 0\ 2](2\ 0\ 5)$ and $[5\ 0\ \overline{2}](2\ 0\ 5)$ will be almost equal. As shown in Fig. 5(a), when the scratch distance is less than 10 μm, the variation of scratch depth for $[\overline{5}\ 0\ 2](2\ 0\ 5)$ and $[5\ 0\ \overline{2}](2\ 0\ 5)$ directions is similar. Since there is no atomic slip resistance $F_{slip}$ in rubbing, the scratch hardness for $[\overline{5}\ 0\ 2](2\ 0\ 5)$ and $[5\ 0\ \overline{2}](2\ 0\ 5)$ directions should both be similar to the indentation hardness at the rubbing stage, as shown in the stage I in Fig. 7(a) and (b). Unlike the ploughing and chipping stages, the difference in COF for $[\overline{5}\ 0\ 2](2\ 0\ 5)$ and $[5\ 0\ \overline{2}](2\ 0\ 5)$ directions in the rubbing stage is mainly due to the difference in lateral hardness rather than the difference in scratch depth.

## 4. Conclusions

In this study, the anisotropy origins of scratch hardness and coefficient of friction for monocrystalline Cu were investigated by scratching along $[\overline{5}\ 0\ 2](2\ 0\ 5)$ and $[5\ 0\ \overline{2}](2\ 0\ 5)$ directions under ramp normal force mode. The main findings obtained by nano-scratching experiments and corresponding MD simulation are summarized as follows:

1) When the normal load or scratch depth is small, the $< 1\ 1\ 1 > \{1\ 1\ 0\}$ slip system is not activated in nano-scratching monocrystalline Cu. In this case, the rubbing dominates the scratching process for both the $[\overline{5}\ 0\ 2](2\ 0\ 5)$ and $[5\ 0\ \overline{2}](2\ 0\ 5)$ scratch directions, whose scratch hardness and COF are similar. Meanwhile, as the scratch depth increases, the scratch hardness and COF in the rubbing stage exhibits a significant size effect.

2) When the scratch depth is relatively large, the $< 1\ 1\ 1 > \{1\ 1\ 0\}$ slip system will be activated in nano-scratching monocrystalline Cu. In this case, the atoms slip along the $< 1\ 1\ 0 > \{1\ 1\ 1\}$ slip system towards the specimen surface. Since the tip hinders the movement of atoms towards the specimen surface, the effective normal force $F_{ef}$ is reduced due to the atomic slip resistance $F_{slip}$ in scratching. When scratching along $[\overline{5}\ 0\ 2](2\ 0\ 5)$ and $[5\ 0\ \overline{2}](2\ 0\ 5)$ directions, the atomic slip resistance $F_{slip}$ for chip formation and ploughing are different, so it exhibits anisotropy of scratch hardness and COF. Generally, the chip formation direction has a larger scratch hardness and a smaller COF than the ploughing direction.

3) Due to the effect of slip resistance $F_{slip}$ in the state of chip and ploughing, the scratch hardness is greater than the indentation hardness. However, in the rubbing stage, the effect of slip resistance $F_{slip}$ on the nano scratching process is relatively small; therefore, the variation of indentation hardness and scratch hardness with respect to depth is similar. In addition, the lateral hardness in the chip state significantly increases with the scratch distance due to the material pile-up in front of the groove in the chip. However, in the plowing stage, the material mainly piles up on both sides of the groove; thus, the lateral hardness slightly increases with the scratch distance.

## Declaration of Competing Interest

The authors declare that they have no known competing financial interests or personal relationships that could have appeared to influence the work reported in this paper.

## Data availability

No data was used for the research described in the article.

## References

[1] Saka N, Eusner T, Chun JH. Nano-scale scratching in chemical-mechanical polishing. CIRP Ann - Manuf Technol 2008;57:341–4. https://doi.org/10.1016/j.cirp.2008.03.098.

[2] Ballarre J, López DA, Cavalieri AL. Frictional and adhesive behavior of organic-inorganic hybrid coatings on surgical grade stainless steel using nano-scratching technique. Wear 2009;266:1165–70. https://doi.org/10.1016/j.wear.2009.03.029.

[3] Graça S, Colaço R, Vilar R. Micro-to-nano indentation and scratch hardness in the Ni-Co system: Depth dependence and implications for tribological behavior. Tribol Lett 2008;31:177–85. https://doi.org/10.1007/s11249-008-9350-1.

[4] Liu X, Zhang B, Wei Y. Interference effect on friction behavior of asperities on single crystal copper. Tribol Int 2015;81:169–78. https://doi.org/10.1016/j.triboint.2014.08.007.

[5] Moshkovich A, Lapsker I, Laihtman A, Rapoport LS. Friction, wear and deformed structure of Ag and Ni under early stages of scratching. Wear 2020;462–463: 203510. https://doi.org/10.1016/j.wear.2020.203510.

[6] Yang X, Qiu Z, Wang Y. Investigation of material flow behaviour and chip formation mechanism during grinding of glass-ceramics by nanoscratch. Ceram Int 2019;45:15954–63. https://doi.org/10.1016/j.ceramint.2019.05.104.

[7] Yang X, Qiu Z, Li X. Investigation of scratching sequence influence on material removal mechanism of glass-ceramics by the multiple scratch tests. Ceram Int 2019;45:861–73. https://doi.org/10.1016/j.ceramint.2018.09.256.

[8] Zhu A, He D, Luo W, Liu Y. Role of crystal orientation on chemical mechanical polishing of single crystal copper. Appl Surf Sci 2016;386:262–8. https://doi.org/10.1016/j.apsusc.2016.06.030.

[9] Fu WE, Chen CCA, Huang KW, Chang YQ, Lin TY, Chang CS, et al. Nano-scratch evaluations of copper chemical mechanical polishing. Thin Solid Films 2013;529: 306–11. https://doi.org/10.1016/j.tsf.2012.03.057.

[10] Liu M, Zheng Q, Gao C. Sliding of a diamond sphere on fused silica under ramping load. Mater Today Commun 2020;25:101684. https://doi.org/10.1016/j.mtcomm.2020.101684.

[11] Beake BD, Harris AJ, Liskiewicz TW. Review of recent progress in nanoscratch testing. Tribol - Mater Surf Interfaces 2013;7:87–96. https://doi.org/10.1179/1751584×13Y.0000000037.

[12] Tsybenko H, Farzam F, Dehm G, Brinckmann S. Scratch hardness at a small scale: Experimental methods and correlation to nanoindentation hardness. Tribol Int 2021;163:107168. https://doi.org/10.1016/j.triboint.2021.107168.

[13] Ichimura H, Rodrigo A. The correlation of scratch adhesion with composite hardness for TiN coatings. Surf Coat Technol 2000;126:152–8. https://doi.org/10.1016/S0257-8972(00)00541-7.

[14] Adler TA, Walters RP. Wear and scratch hardness of 304 stainless steel investigated with a single scratch test. Wear 1993;162–164:713–20. https://doi.org/10.1016/0043-1648(93)90071-S.

[15] Kareer A, Hou XD, Jennett NM, Hainsworth SV. The existence of a lateral size effect and the relationship between indentation and scratch hardness in copper. Philos Mag 2016;96:3396–413. https://doi.org/10.1080/14786435.2016.1146828.

[16] Brookes CA, Green P, Harrison PH, Moxley B. Some observations on scratch and indentation hardness measurements. J Phys D Appl Phys 1972;5:1284–93. https://doi.org/10.1088/0022-3727/5/7/313.

[17] Brookes CA. Scratch and indentation hardness of crystals. Philos Mag A Phys Condens Matter, Struct Defects Mech Prop 1981;43:529–43. https://doi.org/10.1080/01418618108240393.

[18] Zhang G, Han J, Chen Y, Xiong J, Wang J, Ran J. Generation mechanism and dual-dynamics simulation of surface patterns in single-point diamond turning of single-crystal copper. J Manuf Process 2022;75:1023–38. https://doi.org/10.1016/j.jmapro.2022.01.052.

[19] Chavoshi SZ, Gallo SC, Dong H, Luo X. High temperature nanoscratching of single crystal silicon under reduced oxygen condition. Mater Sci Eng A 2017;684:385–93. https://doi.org/10.1016/j.msea.2016.11.097.

[20] Zhang S, Guo X, Jin Z, Kang R, Guo D, Tang WC. Surface morphologies and corresponding hardness evolution during nanoscratching. J Mater Res Technol 2020;9:3179–89. https://doi.org/10.1016/j.jmrt.2020.01.064.

[21] Lee K, Marimuthu KP, Kim CL, Lee H. Scratch-tip-size effect and change of friction coefficient in nano / micro scratch tests using XFEM. Tribol Int 2018;120:398–410. https://doi.org/10.1016/j.triboint.2018.01.003.

[22] Peng LF, Mao MY, Fu MW, Lai XM. Effect of grain size on the adhesive and ploughing friction behaviours of polycrystalline metals in forming process. Int J Mech Sci 2016;117:197–209. https://doi.org/10.1016/j.ijmecsci.2016.08.022.

[23] Li K, Shapiro Y, Li JCM. Scratch test of soda-lime glass. Acta Mater 1998;46:5569–78. https://doi.org/10.1016/S1359-6454(98)00163-3.

[24] Zhu J, Xiong C, Ma L, Zhou Q, Huang Y, Zhou B, et al. Coupled effect of scratching direction and speed on nano-scratching behavior of single crystalline copper. Tribol Int 2020;150. https://doi.org/10.1016/j.triboint.2020.106385.

[25] Zhu J, Li X, Zhou Q, Aghababaei R. On the anisotropic scratching behavior of single crystalline copper at nanoscale. Tribol Int 2022;175:107794. https://doi.org/10.1016/j.triboint.2022.107794.

[26] Wang Z, Zhang H, Li Z, Li G, Zhang J, Zhang J, et al. Crystal plasticity finite element simulation and experiment investigation of nanoscratching of single crystalline copper. Wear 2019;430–431:100–7. https://doi.org/10.1016/j.wear.2019.04.024.

[27] Sharma A, Datta D, Balasubramaniam R. Molecular dynamics simulation to investigate the orientation effects on nanoscale cutting of single crystal copper. Comput Mater Sci 2018;153:241–50. https://doi.org/10.1016/j.commatsci.2018.07.002.

[28] Hu J, Liu X, Wei Y. Effect of plasticity and adhesion on the stick-slip transition at nanoscale friction. Tribol Int 2021;164:107230. https://doi.org/10.1016/j.triboint.2021.107230.

[29] Xu N, Han W, Wang Y, Li J, Shan Z. Nanoscratching of copper surface by CeO2. Acta Mater 2017;124:343–50. https://doi.org/10.1016/j.actamat.2016.11.008.

[30] Liu H, Guo Y, Li D, Wang J. Material removal mechanism of FCC single-crystalline materials at nano-scales: Chip removal & ploughing. J Mater Process Technol 2021;294:117106. https://doi.org/10.1016/j.jmatprotec.2021.117106.

[31] Liu H, Guo Y, Zhao P. Surface generation mechanism of monocrystalline materials under arbitrary crystal orientations in nanoscale cutting. Mater Today Commun 2020;25:101505. https://doi.org/10.1016/j.mtcomm.2020.101505.

[32] Plimpton S. Computational limits of classical molecular dynamics simulations. Comput Mater Sci 1995;4:361–4. https://doi.org/10.1016/0927-0256(95)00037-1.

[33] Wang Q, Bai Q, Chen J, Guo Y, Xie W. Stress-induced formation mechanism of stacking fault tetrahedra in nano-cutting of single crystal copper. Appl Surf Sci 2015;355:1153–60. https://doi.org/10.1016/j.apsusc.2015.06.176.

[34] Zhao P, Wu J, Chen H, Liu H, Li D, Tan J. Molecular dynamics simulation study of interaction mechanism between grain boundaries and subgrain boundaries in nano-cutting. J Manuf Process 2021;67:418–26. https://doi.org/10.1016/j.jmapro.2021.04.075.

[35] Faken D, Jónsson H. Systematic analysis of local atomic structure combined with 3D computer graphics. Comput Mater Sci 1994;2:279–86. https://doi.org/10.1016/0927-0256(94)90109-0.

[36] Stukowski A. Visualization and analysis of atomistic simulation data with OVITO-the Open Visualization Tool. Model Simul Mater Sci Eng 2010:18. https://doi.org/10.1088/0965-0393/18/1/015012.